THE JOURNAL OF PHYSICAL CHEMISTRY A

pubs.acs.org/JPCA Article

Dispersion-Corrected DFT Methods for Applications in Nuclear Magnetic Resonance Crystallography

Sean T. Holmes, Cameron S. Vojvodin, and Robert W. Schurko*

Cite This: J. Phys. Chem. A 2020, 124, 10312–10323 Read Online

ACCESS | Metrics & More | Article Recommendations | Supporting Information

ABSTRACT: Nuclear electric field gradient (EFG) tensor parameters depend strongly on electronic structures, making their calculation from first principles an excellent metric for the prediction, refinement, and optimization of crystal structures. Here, we use plane-wave density functional theory (DFT) calculations of EFG tensors in organic solids to optimize the Grimme (D2) and Tkatchenko–Scheffler (TS) atomic-pairwise force field dispersion corrections. Refinements using these new force field correction methods result in better representations of true crystal structures, as gauged by calculations of 177 ^{14}N, ^{17}O, and ^{35}Cl EFG tensors from 95 materials. The most striking result is the degree by which calculations of ^{35}Cl EFG tensors of chloride ions match with experiment, due to the ability of these new methods to properly locate the positions of hydrogen atoms participating in H···Cl$^-$ hydrogen bonds. These refined structures also feature atomic coordinates that are more similar to those of neutron diffraction structures than those obtained from calculations that do not employ the optimized force fields. Additionally, we assess the quality of these new energy-minimization protocols for the prediction of ^{15}N magnetic shielding tensors and unit cell volumes, which complement the larger analysis using EFG tensors, since these quantities have different physical origins. It is hoped that these results will be useful in future nuclear magnetic resonance (NMR) crystallographic studies and will be of great interest to a wide variety of researchers, in fields including NMR spectroscopy, computational chemistry, crystallography, pharmaceutical sciences, and crystal engineering.

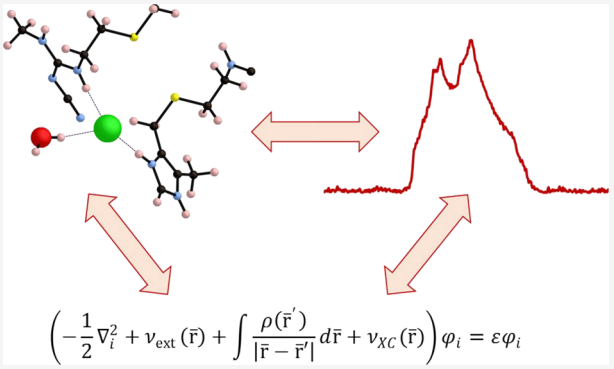

1. INTRODUCTION

The prediction, refinement, and optimization of crystal structures from first principles are ongoing challenges in computational chemistry,[1−3] due to their reliance on accurate modeling of intermolecular noncovalent interactions such as dispersion forces and hydrogen bonding,[4] which are approximately two orders of magnitude weaker than covalent interactions between atoms.[5] Nonetheless, weak noncovalent interactions play crucial roles in determining the molecular-level structures of solids.[6−8] Although it is well known that standard density functional theory (DFT) approximations do not describe long-range dispersion interactions adequately,[9,10] semi-empirical force field corrections can be used to account for these effects. Because of advances in this field, first principles prediction of crystal structures is a significant driving force behind materials discovery[11] and therefore has wide ranging applications in fields related to crystal engineering.[12]

The assessment of structural models resulting from first principles structure prediction or the refinement of diffraction data is often accomplished by comparing thermodynamic criteria, such as static lattice energies. Computational studies have demonstrated that the relative energies between stable solid forms are typically small. Differences in static lattice energies between stable polymorphs are less than 7.2 kJ mol^{-1} in 95% of cases and less than ca. 2 kJ mol^{-1} in 50% of cases.[13] Similarly, enthalpies of cocrystallization are ca. −8 kJ mol^{-1} on average (i.e., cocrystals are stabilized by 8 kJ mol^{-1} relative to their constituent coformers).[14] Because of these small differences in energy and the computational challenges associated with calculating these energetic differences reliably and precisely, alternative methods of structural validation are desirable.

Nuclear magnetic resonance (NMR) crystallography has emerged as an important tool for assessing the quality of crystal structures because of the inherent relationships between molecular-level structures and parameters determined by solid-state NMR (SSNMR) spectroscopy.[15] Instead of relying on calculations of thermodynamic quantities such as differences in enthalpy or free energy, NMR crystallographic investigations are often aided by subjecting proposed

Received: July 12, 2020
Revised: November 5, 2020
Published: December 1, 2020

https://dx.doi.org/10.1021/acs.jpca.0c06372
J. Phys. Chem. A 2020, 124, 10312–10323

structures to computational modeling of NMR parameters using DFT. The combination of SSNMR spectroscopy and DFT calculations can be used to complement, or even replace,[15−17] the assessment of structures through thermodynamic considerations.

There are several NMR interactions that provide information on molecular-level structures, including the chemical shift, indirect spin−spin coupling, direct dipolar coupling, and quadrupolar interactions. Careful measurements of dipolar coupling constants can provide distances between spins; this approach has been used to determine the structures of organic solids in combination with powder X-ray diffraction (XRD) methods.[18,19] Similarly, REDOR and double quantum recoupling methods have been used to obtain distance and conformation constraints to aid in the solutions of crystal structures in combination with powder XRD.[20−23] Chemical shifts, whether the isotropic chemical shift or the principal values of the chemical shift tensor, are the most common quantities used to assess the quality of a crystal structure because they provide a data set that is rich in information on electronic structures. Successes in NMR crystallography that involve the measurements of chemical shifts include the determination of partial and/or complete crystal structures,[24−31] including thermal ellipsoids in certain cases.[29] Practical considerations associated with the predictions of magnetic shielding tensors for nuclides commonly found in organic crystals (^{1}H, ^{13}C, ^{15}N, ^{17}O, ^{19}F, etc.) have been discussed in detail,[32−38] including their implications for NMR crystallography.[39−45]

Analysis of NMR powder patterns of quadrupolar nuclides (nuclear spin $I > 1/2$) can provide information on nuclear electric field gradient (EFG) tensors. EFG tensors are sensitive to even the smallest changes and/or differences in molecular-level structures, making the calculation of these quantities a robust method for assessing the quality of crystal structures.[46] In organic solids, the most common quadrupolar nuclides are ^{14}N[47−59] and ^{17}O,[48,60−77] both of which have been used in NMR and NQR crystallographic investigations. However, organic molecules often crystallize as salts; in such cases, analysis of the quadrupolar powder patterns of the counterion can provide key information on intermolecular interactions. ^{35}Cl EFG tensors are especially relevant in this regard[58,78−88] because approximately half of solid-state active pharmaceutical ingredients used in oral dosage forms are manufactured as HCl salts.[89] Chloride ions are typically involved in complex networks of hydrogen bonds with nearby hydrogen-donating moieties. The values of the principal components of the EFG tensor are influenced strongly by the precise positions of the hydrogen atoms. In contrast to chemical shifts, EFG tensor parameters are generally more sensitive to longer-range interactions. Furthermore, because EFG tensors are dependent only on ground-state electron densities, they can be calculated more rapidly than chemical shifts, making them highly suitable for the purpose of structural screening.

The use of dispersion-corrected DFT approximations is necessary to refine the crystal structures of organic solids such that calculations on the energy-minimized structures result in accurate EFG tensors. The effects of dispersion can be incorporated into plane-wave DFT calculations through force field correction models that depend on a set of atomic coordinates. These force field corrections contain empirical parameters that, in principle, can be adjusted or refined through benchmarking against experimental data.[90,91] The most common type of experimental data used to evaluate the performance of force field correction protocols is sublimation enthalpy, although other quantities such as unit cell volumes, bulk moduli, and vibrational lattice modes are also employed.[92,93] However, we have recently demonstrated that force field correction models can be reparameterized through calculations of EFG tensors.[94,95] This preliminary result was limited to a reparameterization of the Grimme D2 force field, although the proposed methodology could be extrapolated to other force field models, potentially leading to more accurate predictions of EFG tensors and more reliable crystal structures.

Herein, we demonstrate the reparameterization of atomic-pairwise dispersion force field corrections of Grimme (D2)[96] and Tkatchenko and Scheffler (TS)[97] through calculations of ^{14}N, ^{17}O, and ^{35}Cl EFG tensor parameters in neutral organic molecules and chloride salts. The crystal structures refined with these newly parameterized dispersion-corrected plane wave DFT methods result in superior crystal structures to those determined by XRD methods, as determined by the better agreement with 177 experimental EFG tensor parameters from 95 materials (45 neutral organic solids and 50 organic chloride salts). The new structural refinement protocols are assessed for the prediction of ^{15}N chemical shift tensors, which complements the analysis based on EFG tensors since these two interactions have independent physical origins. Finally, these protocols are assessed for the refinements of unit cell volumes of neutral molecules (using the X23 test set)[98,99] and organic chloride salts.

2. COMPUTATIONAL DETAILS

2.1. Geometry Optimizations. All calculations were performed on models of structures determined from XRD methods. Structural refinements employed plane-wave DFT, as implemented in the CASTEP module of BIOVIA Materials Studio 2018.[100,101] Structural refinements employed the Quasi-Newton Broyden−Fletcher−Goldfarb−Shanno energy-minimizing scheme.[102] The RPBE density functional was used in all of these calculations;[103] this functional has been demonstrated to work well for the structural refinement of organic solids and the prediction of NMR parameters for light atoms.[80,81,95,104,105] The calculations modeled core-valence interactions using ultrasoft pseudopotentials generated on the fly,[106] used a plane-wave cutoff energy of 700 eV, and evaluated integrals over the Brillouin zone with a Monkhorst-Pack grid with a k-point spacing of 0.07 Å^{-1}. Where indicated, dispersion was included using the semiempirical two-body models D2 and TS.[96,97,107] The thresholds for structural convergence included a maximum change in energy of 5×10^{-6} eV atom^{-1}, a maximum displacement of 5×10^{-4} Å atom^{-1}, a maximum Cartesian force of 10^{-2} eV Å^{-1}, and a maximum stress of 2×10^{-2} GPa. All of the energy minimized structures are provided in the Supporting Information.

2.2. Calculations of NMR Tensor Parameters. Nuclear EFG tensors were computed for periodic models of the solids using CASTEP,[108] with the same criteria as the geometry optimizations. Nitrogen magnetic shielding tensors were calculated using both periodic and cluster-based approaches. The former set of calculations was carried out using the GIPAW formalism as implemented in CASTEP with the RPBE functional[109] (*N.B.*: the inclusion of the dispersion force field does not influence the algorithms by which the EFG or magnetic shielding tensors are evaluated in CASTEP). The latter calculations were carried out using Amsterdam Density

https://dx.doi.org/10.1021/acs.jpca.0c06372
J. Phys. Chem. A 2020, 124, 10312−10323

Functional (ADF 2017) with the GIAO formalism.[110] Clusters were constructed using the procedures outlined in previous work[32−34] and consisted of a central molecule surrounded by a sphere of least 13 additional molecules (a list of atomic coordinates are provided in the Supporting Information). The clusters corresponding to L-histidine $HCl{\cdot}H_2O$ and glycylglycine $HCl{\cdot}H_2O$ had net charges of +3 and +5, respectively. These calculations used the hybrid functional PBE0.[111] A basis set partitioning scheme was used in which the central molecule is given a locally dense TZ2P basis set and all other molecules are given the smaller DZ basis set.

2.3. Analysis of EFG Tensors. EFGs with their origin at a nuclear center are described by symmetric, traceless, second-rank tensors with principal components V_{kk}, k = 1, 2, 3, defined such that $|V_{33}| \geq |V_{22}| \geq |V_{11}|$. The interaction between the nuclear electric quadrupole moment and the EFG tensor is specified by the quadrupolar coupling constant (C_Q) and the asymmetry parameter (η_Q):

$$C_Q = eQV_{33}/h \tag{1}$$

$$\eta_Q = (V_{11} - V_{22})/V_{33} \tag{2}$$

In the above expressions, e is the elementary charge, h is Planck's constant, and Q is the nuclear quadrupole moment [$Q(^{14}N)$ = 2.044 fm^2, $Q(^{17}O)$ = −2.558 fm^2, and $Q(^{35}Cl)$ = −8.165 fm^2].[112] In typical single-resonance SSNMR experiments, the signs of the principal components of the EFG tensor cannot be determined; however, the signs are available from first principles calculations.

We assess the agreement between an experimental ($V_{kk}^{m,\,exp}$, k = 1, 2, 3) and calculated ($V_{kk}^{m,\,calc}$) EFG tensor at nucleus m using the *EFG distance* (Γ_m) metric. The EFG distance quantifies the degree of similarity between two sets of the principal components of EFG tensors (here, one experimental and one computed set of tensors) using a single scalar value (in a.u.):

$$\Gamma_m = \left(\frac{1}{15}[3\Delta_{11}^2 + 3\Delta_{22}^2 + 3\Delta_{33}^2 + 2\Delta_{11}\Delta_{22} + 2\Delta_{11}\Delta_{33} + 2\Delta_{22}\Delta_{33}]\right)^{1/2} \tag{3}$$

$$\Delta_{kk} = |V_{kk}^{m,calc}| - |V_{kk}^{m,exp}| \tag{4}$$

This metric is analogous to the chemical shift distance introduced by Grant and coworkers.[113] A root-mean-square EFG distance for an ensemble of M EFG tensors (Γ_{RMS}) is determined by the following expression:

$$\Gamma_{RMS} = \left(\frac{1}{M}\sum_m \Gamma_m^2\right)^{1/2} \tag{5}$$

2.4. Analysis of Nitrogen Magnetic Shielding Tensors. The relationship between experimental principal components of ^{15}N chemical shift tensors ($\delta_{kk}^{m,\,exp}$) and calculated principal components of nitrogen magnetic shielding tensors ($\sigma_{kk}^{m,\,calc}$) is modeled by the following expression:

$$\sigma_{kk}^{m,calc} = A\delta_{kk}^{m,exp} + B \tag{6}$$

Here, coefficients A and B are the slope of the correlation line and the interpolated shielding of the reference system (nitromethane at δ_{iso} = 0.0 ppm), respectively. Using this correlation, one can obtain calculated principal components of the chemical shift tensors.

$$\delta_{kk}^{m,calc} = (B - \sigma_{kk}^{m,calc})/|A| \tag{7}$$

The agreement between experimental and calculated nitrogen chemical shift tensors for atom m is given by the chemical shift distance (Δ_m), and the agreement for an ensemble of M atoms is given by the RMS chemical shift distance (Δ_{RMS}, see the Supporting Information for details).[113]

3. RESULTS AND DISCUSSION

3.1. Overview. Herein, we refine the crystal structures of molecular solids using semiempirical dispersion-corrected plane-wave DFT methods and assess the quality of the resulting energy-minimized structures through calculations of NMR interaction tensor parameters. The optimization of parameters within the force field corrections is assessed via comparison between experimental and calculated principal components of EFG tensors from a *training set* of molecular solids. The applicability of the structural refinement protocols is evaluated by calculation of the EFG tensors of a larger *test set* of molecular solids. These structural refinement protocols are also assessed for the calculation of the principal components of nitrogen magnetic shielding tensors. Finally, we compare these structural refinement protocols in terms of differences between the energy-minimized structures when the unit cell volumes relaxed; this latter consideration is especially important for NMR crystallographic studies in which initial structures are proposed through ab initio crystal structure prediction, rather than XRD methods.

3.2. Force Field Parameterization. In the Grimme (DFT-D2) two-body dispersion model,[96] the dispersion energy (E_{disp}) is computed as an atomic-pairwise correction to the Kohn−Sham energy (E_{KS}):

$$E_{DFT-D2} = E_{KS} + E_{disp} \tag{8}$$

The dispersion energy is computed in a comparable manner in the Tkatchenko−Scheffler (DFT-TS) model.[97] In both models, the dispersion energy is defined by the following unscaled expression:

$$E_{disp} = -\sum_{i,j>1}^{N} \frac{c_{6,ij}}{R_{ij}^6} f_{damp}(R_{ij}) \tag{9}$$

The indices i and j denote atom pairs within the N interacting atoms, $c_{6,ij}$ is the coefficient of the leading term in the London series,[96] and R_{ij} is the interatomic distance. The Fermi-type damping function, $f_{damp}(R_{ij})$, modulates the effective range and steepness of the dispersion interaction:

$$f_{damp}(R_{ij}) = \frac{1}{1 + \exp\left[-d\left(\frac{R_{ij}}{R_0} - 1\right)\right]} \tag{10}$$

In this expression, R_0 is the sum of the van der Waals' radii of atom pair ij, and d is a damping parameter; the latter parameter specifies how sharply the dispersion interaction tends toward zero for small values of R_{ij}/R_0. In the DFT-D2 model, the dispersion coefficients and van der Waals' radii are constants; in the DFT-TS model, they are dependent on the charge density, lending additional flexibility to the force field for application to atoms in differing chemical environments.

https://dx.doi.org/10.1021/acs.jpca.0c06372
J. Phys. Chem. A 2020, 124, 10312−10323

Here, the value of the damping parameter was optimized through comparison of experimental and calculated principal components of 20 ^{14}N, 21 ^{17}O, and 9 ^{35}Cl EFG tensors (Figure 1).[94,95] This optimization was accomplished through calcu-

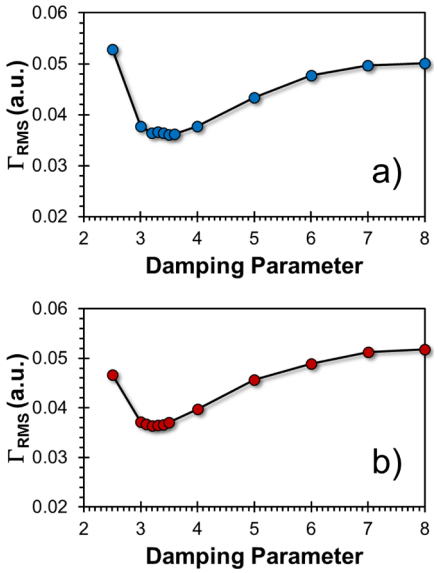

Figure 1. RMS EFG distances (Γ_{RMS}) between experimental and calculated principal components of the EFG tensors of the training set organic solids as a function of the damping parameter. By default, the value of d is set to 20 in CASTEP. The optimizations are illustrated for the (a) RPBE-D2 and (b) RPBE-TS methods.

lations on a training set consisting of neutral organic molecules and HCl salts, including urea, uracil, cytosine, imidazole, glycine (three polymorphs), L-alanine, L-valine, taurine, glycine HCl, L-alanine HCl, L-valine HCl, L-threonine HCl, L-histidine HCl·H_2O, L-cysteine HCl·H_2O, L-glutamic acid HCl, cytosine HCl, aminoguanidine HCl, and dopamine HCl. In all cases, a comparison was made between experimental determinations of EFG tensor parameters made at room temperature and calculations on crystal structures obtained at room temperature. The unit cell volumes remained fixed in all calculations. The agreement with experiment was assessed using the value of Γ_{RMS} for all 50 EFG tensors in the training set. In a series of structural refinements on the training set organic solids, the value of the damping parameter was modulated over the range of $2.5 \leq d \leq 20$. The damping parameter was incremented in steps of $\Delta d = 0.1$ near the region of the optimized value and with larger increments ($0.1 \leq \Delta d \leq 1.0$) in other regions. Minimum values for Γ_{RMS} are obtained from the training set when the damping parameter is fixed at values of $d = 3.5$ and $d = 3.3$ for the RPBE-D2 and RPBE-TS methods, respectively (Figure 2, Table 1). The optimized value of the damping parameter for the D2 force field is consistent with our previous work.[94,95] Subsequently, all calculations using the new parameterization of the damping parameter are denoted as the RPBE-D2* and RPBE-TS* models, whereas calculations using $d = 20$ (the default value in CASTEP) are referred to as the RPBE-D2 and RPBE-TS models.

3.3. Calculations of EFG Tensors. The aforementioned force field correction models were applied for the DFT energy minimization of the crystal structures of a large test set of organic molecules and the subsequent calculation of the nuclear EFG tensor parameters (Figures 2 and 3, Tables S1–

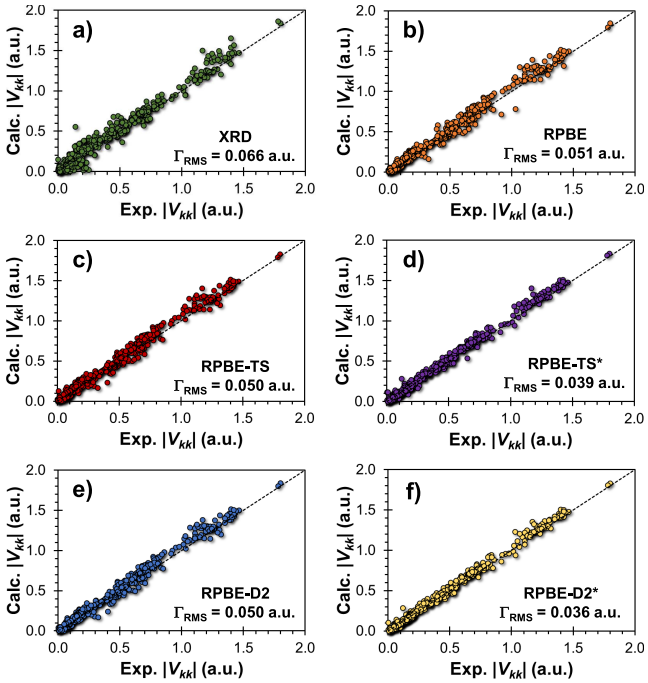

Figure 2. Relationships between the principal components of calculated and experimental nuclear EFG tensors. Results are shown for the principal components of the 177 EFG tensors in the training and test sets. Each panel illustrates a different type of structural data used in the calculations of the EFG tensor parameters, including (a) XRD-derived structures, as well as structures that have been optimized at the (b) RPBE, (c) RPBE-TS, (d) RPBE-TS*, (e) RPBE-D2, and (f) RPBE-D2* levels. The dashed lines represent perfect agreement between calculated and experimental values.

Table 1. Values of Γ_{RMS} (a.u.) Associated with the Prediction of EFG Tensors for the Training and Test Sets of Organic Solids

nuclide	N^a	XRD	RPBE	RPBE-TS	RPBE-D2	RPBE-TS*	RPBE-D2*
Training Set							
^{14}N	20	0.065	0.031	0.035	0.029	0.035	0.027
^{17}O	21	0.075	0.071	0.070	0.070	0.050	0.050
^{35}Cl	9	0.052	0.043	0.046	0.042	0.008	0.009
Total	50	0.067	0.053	0.054	0.052	0.039	0.037
Test Set							
^{14}N	47	0.064	0.034	0.035	0.035	0.033	0.033
^{17}O	38	0.084	0.074	0.069	0.070	0.060	0.054
^{35}Cl	42	0.043	0.038	0.039	0.037	0.015	0.011
Total	127	0.065	0.051	0.049	0.048	0.039	0.036
Both Sets							
^{14}N	67	0.064	0.033	0.035	0.033	0.033	0.031
^{17}O	59	0.081	0.073	0.070	0.070	0.056	0.052
^{35}Cl	51	0.044	0.039	0.041	0.038	0.014	0.011
Total	177	0.066	0.051	0.050	0.050	0.039	0.036

[a] N refers to the number of EFG tensors in the training set, test set, or combination of both sets; this value is lower for the XRD-derived structures because the positions of the hydrogen atoms were not always reported.

S6, Figures S1–S3). The test set consists of 42 ^{35}Cl sites, 38 ^{17}O sites, and 47 ^{14}N sites. Altogether, the combined training and test sets consist of the principal components of 177 EFG tensors. Fewer systems are considered for calculations on

https://dx.doi.org/10.1021/acs.jpca.0c06372
J. Phys. Chem. A 2020, 124, 10312–10323

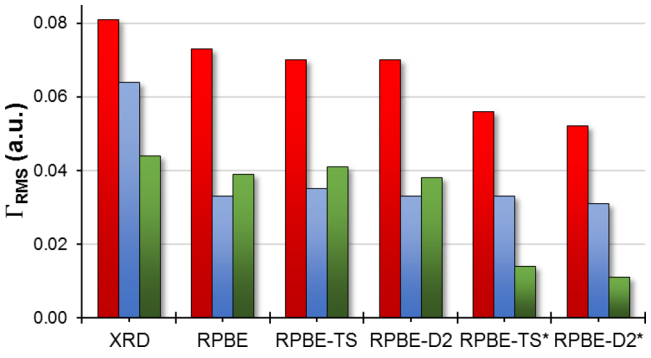

Figure 3. RMS EFG distances (Γ_{RMS}) between experimental and calculated principal components of the EFG tensors for individual types of atoms in the training and test set organic solids. Results are shown for ^{17}O (red), ^{14}N (blue), and ^{35}Cl (green) EFG tensor parameters.

structures determined by XRD methods because some of these studies report unrealistic positions for the hydrogen atoms or do not report the positions of hydrogen atoms at all.

A statistical analysis of the calculated EFG tensor parameters is provided in Table 1. For all 177 EFG tensors in the training and test sets, the best agreement with experiment was obtained from structures refined at the RPBE-TS* and RPBE-D2* levels; the values of Γ_{RMS} for these models are 0.039 and 0.036 a.u., respectively. The RPBE, RPBE-TS, and RPBE-D2 structural refinement methods led to similar Γ_{RMS} values between 0.051 and 0.050 a.u. The worst agreement with experiment was obtained from the XRD-derived structures, with a value of Γ_{RMS} of 0.066 a.u.

The ^{35}Cl EFG tensors at chloride ion sites are the most strongly affected by structural refinement. For both sets, the lowest value of $\Gamma_{RMS}(^{35}Cl)$ is obtained for RPBE-D2* (0.011 a.u.) and RPBE-TS* (0.014 a.u.) structures. This represents a substantial improvement over all other structural refinement models, for which values of $\Gamma_{RMS}(^{35}Cl)$ fall between 0.038 and 0.041 a.u., and over XRD-derived structures, for which the value of $\Gamma_{RMS}(^{35}Cl)$ is 0.044 a.u. Experimental uncertainties in $C_Q(^{35}Cl)$ are typically in the order of 0.003 a.u; the differences in $\Gamma_{RMS}(^{35}Cl)$ values between different structural refinement protocols tend to be one order of magnitude larger than this. The large errors in the prediction of ^{35}Cl EFG tensors for certain types of structures appear to reflect difficulties in positioning the hydrogen atoms. Chloride anions in organic solids participate in intricate networks of H···Cl^- hydrogen bonds that influence their ^{35}Cl EFG tensors; these interactions must be modeled satisfactorily in the calculations to obtain reasonable agreement with experimental values. All methods other than RPBE-TS* and RPBE-D2* tend to underestimate the lengths of the H···Cl^- hydrogen bonds, leading to significant overestimations in the magnitudes of the principal components of the chlorine EFG tensors.

The ^{14}N and ^{17}O EFG tensors at covalently bonded N and O sites are also affected by geometry optimizations, although the effects are generally smaller than those observed for the aforementioned ^{35}Cl EFG tensors. For the ^{17}O sites, the lowest value of $\Gamma_{RMS}(^{17}O)$ is obtained for RPBE-D2* (0.052 a.u.) and RPBE-TS* (0.056 a.u.) structures. In contrast, RPBE, RPBE-TS, and RPBE-D2 structures all lead to values of $\Gamma_{RMS}(^{17}O)$ between 0.070 and 0.073 a.u., whereas XRD-derived structures result in a $\Gamma_{RMS}(^{17}O)$ of 0.081 a.u. ^{14}N EFG tensors appear to be the least affected by the method of geometry optimization. For XRD-derived structures, we report $\Gamma_{RMS}(^{14}N) = 0.064$ a.u., whereas this value falls between 0.031 and 0.035 a.u. for all refined structures. The lowest values of $\Gamma_{RMS}(^{14}N)$ are associated with the RPBE-D2* structures.

Further differences between the structural refinement protocols becomes evident from a closer consideration of pseudotetrahedral nitrogen-containing moieties; in particular, the degree to which the ^{14}N EFG tensor is influenced by geometry optimization is highly dependent upon the presence of intermolecular hydrogen bonding involving the N-containing moiety (Table S7). Pseudotetrahedral nitrogen sites with high values of η_Q ($0.71 \leq \eta_Q \leq 1.00$; $|V_{22}| \approx |V_{33}|$) are typically found in $RR'NH_2^+$ groups. Here, the distinct principal component of the ^{14}N EFG tensor, V_{11}, is oriented within/near the H−N−H plane. The calculated values of the ^{14}N EFG tensors of these sites do not appear to be affected strongly by the choice of energy-minimization protocol, as reflected by values of $\Gamma_{RMS}(^{14}N)$ falling between 0.035 and 0.038 a.u. in all cases. Pseudotetrahedral nitrogen sites with low values of η_Q ($0.00 \leq \eta_Q \leq 0.30$; $V_{11} \approx V_{22}$) typically correspond to RNH_3^+ groups that do not participate in intermolecular hydrogen bonding. The unique principal component of the ^{14}N EFG tensor, V_{33}, is nearly coincident with the R−N bonding axis. The magnitudes of V_{11} and V_{22} are comparable, indicating that neither principal component is influenced strongly by the effects of intermolecular hydrogen bonding. This is reflected in the observation that the calculated EFG tensors of these sites are not influenced strongly by the choice of energy-minimization protocol because all values of $\Gamma_{RMS}(^{14}N)$ fall between 0.022 and 0.025 a.u. In contrast, pseudotetrahedral nitrogen sites featuring an intermediate value of η_Q ($0.31 \leq \eta_Q \leq 0.70$; $V_{11} \neq V_{22}$) are typically found in RNH_3^+ groups that are influenced significantly by hydrogen bonds. In particular, the N−H bonds have slightly different lengths such that the unique principal component, V_{33}, is oriented away from the R−N bonding axis but still is directed toward the C atom. For these nitrogen sites, the value of $\Gamma_{RMS}(^{14}N)$ is affected by the choice of energy minimization protocol, with values falling between 0.018 and 0.032 a.u. The best agreement with experiment is obtained for structures refined at the RPBE-D2* level, whereas the worst agreement is obtained at the RPBE and RPBE-TS levels.

3.4. Comparison with Neutron Diffraction Structures.

The quality of crystal structures derived from neutron diffraction (ND) often surpasses that of XRD-derived structures because hydrogen atoms only scatter X-rays weakly, leading to systematic shortenings of bond lengths.[114] This consideration is particularly important for computing the ^{35}Cl EFG tensors of chloride ions since they are influenced by the positions of nearby hydrogen atoms, particularly those participating in H···Cl^- hydrogen bonds.[79,81,94,95] Six materials have been characterized previously by both room-temperature ND and ^{35}Cl SSNMR spectroscopy: (i) glycine HCl, (ii) L-valine HCl, (iii) L-phenylalanine HCl, (iv) L-glutamic acid HCl, (v) L-lysine HCl·$2H_2O$ (two independent structural determinations), and (vi) L-histidine HCl·H_2O.[115−121] Calculations of the ^{35}Cl EFG tensors for the ND-derived structures afford an additional figure of merit for assessing the various types of structures considered here (Figure 4, Table S8). For each system, the best agreement with experiment is obtained from structures refined with the RPBE-D2* and RPBE-TS* methods.

https://dx.doi.org/10.1021/acs.jpca.0c06372
J. Phys. Chem. A 2020, 124, 10312−10323

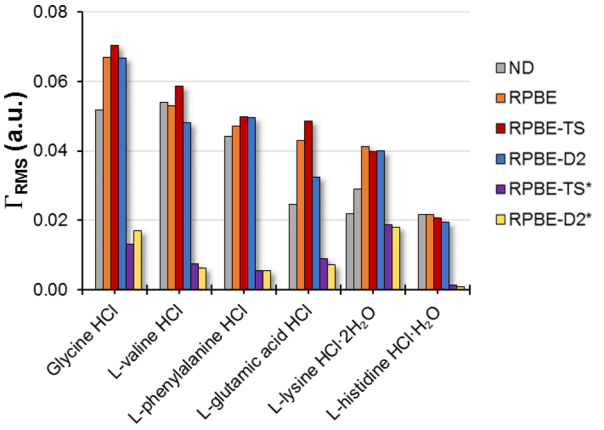

Figure 4. ^{35}Cl RMS EFG distances (Γ_{RMS}) between experimental and calculated principal components of EFG tensors. Calculations are based on structural models determined by ND and various refinements of XRD-derived structures.

Differences between crystal structures can be quantified by root-mean-square Cartesian displacements (RMSCDs).[3,122] Crystal structures of these HCl salts refined at the RPBE-D2* and RPBE-TS* are the most similar to the ND structures, with average RMSCD values of 0.029 and 0.027 Å, respectively. In contrast, RPBE-TS structures are the most dissimilar from the ND structures, with an average RMSCD value of 0.045 Å. Therefore, structures refined at the RPBE-D2* and RPBE-TS* levels are the most similar to ND structures and also provide the most accurate calculations of ^{35}Cl EFG tensors.

3.5. Magnetic Shielding Tensors. Calculations of magnetic shielding tensors are important for gauging the validity of electronic structures because these quantities are influenced by both molecular-level structures and the type of DFT approximation used in the calculation. Here, we present the results of calculations of 42 nitrogen magnetic shielding tensors in organic solids obtained using two DFT functionals (RPBE and PBE0), from structures derived from XRD methods, as well as five types of energy-minimized structures (Figure 5, Table 2, Figures S4 and S5, Tables S9–S11). Calculations of magnetic shielding tensors using the RPBE functional were performed in a periodic framework using the GIPAW approach. In contrast, calculations using the costlier hybrid functional PBE0 (which introduces into the calculation a 25% admixture of Hartree–Fock exchange) were performed using cluster-based models of the extended lattice structure.

Table 2. Statistical Data Associated with the Predictions of Nitrogen Magnetic Shielding Tensors

geometry[a]	shielding[b]	N[c]	B (ppm)	A	$\Delta_{RMS}(^{15}N)$ (ppm)
XRD	RPBE	36	−168.2	−1.123	10.8
RPBE	RPBE	42	−167.8	−1.048	7.5
RPBE-TS	RPBE	42	−167.9	−1.048	7.5
RPBE-D2	RPBE	42	−168.2	−1.048	7.6
RPBE-TS*	RPBE	42	−159.7	−1.074	6.6
RPBE-D2*	RPBE	42	−157.3	−1.070	6.6
XRD	PBE0	36	−161.1	−1.137	11.7
RPBE	PBE0	42	−162.3	−1.070	7.4
RPBE-TS	PBE0	42	−162.4	−1.071	7.4
RPBE-D2	PBE0	42	−162.8	−1.070	7.4
RPBE-TS*	PBE0	42	−152.6	−1.089	6.9
RPBE-D2*	PBE0	42	−150.1	−1.085	6.9

[a]Refers to the type of structural data used in the calculations, i.e., structures determined from X-ray diffraction or one of several plane-wave DFT methods. [b]Refers to the functional used in the calculations of the magnetic shielding tensors. Calculations were performed either using CASTEP (GIPAW) with the RPBE functional or using ADF (GIAO) with the PBE0 functional. [c]N refers to the number of shielding tensors in the training set; this value is lower for the XRD-derived structures because the positions of the hydrogen atoms were not always reported.

The relative performance of these two protocols for modeling the lattice structures of molecular solids for the calculation of nuclear magnetic shielding tensors for many types of atoms has been discussed in previous work; both methods are well established for modeling lattice effects on magnetic shielding tensors.[32−34]

Calculated nitrogen magnetic shielding tensors appear to be more sensitive to the type of structural data used in the calculation than to the choice of functional. In particular, the poorest agreement with experiment is obtained from calculations on XRD-derived structures in which values of $\Delta_{RMS}(^{15}N)$ of 10.8 and 11.7 ppm are obtained for the RPBE and PBE0 functionals, respectively. Refinement of the crystal structures at any level brings the calculated nitrogen magnetic shielding tensors into closer agreement with experiment. Structural refinements at the RPBE, RPBE-D2, and RPBE-TS levels perform similarly for the prediction of nitrogen magnetic shielding tensors; in every case, values of $\Delta_{RMS}(^{15}N)$ range between 7.4 and 7.6 ppm. The best agreement with experiment is obtained when the crystal structures are refined at the RPBE-D2* and RPBE-TS* levels. In these cases, calculations of the nitrogen magnetic shielding tensors using the RPBE and

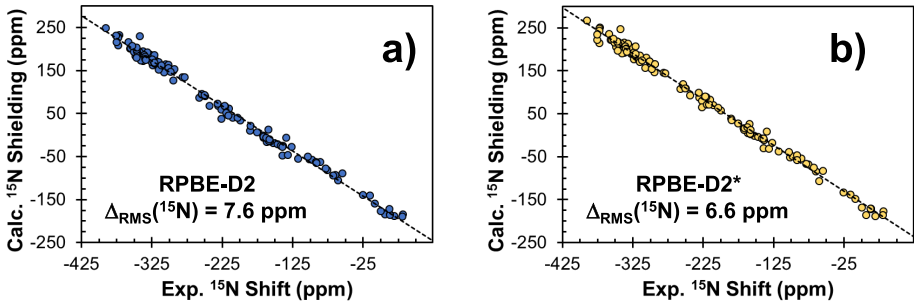

Figure 5. Comparison between principal components of calculated magnetic shielding tensors and experimental principal components of ^{15}N chemical shift tensors. Calculations were performed on structures refined at the (a) RPBE-D2 and (b) RPBE-D2* levels. Magnetic shielding tensors were calculated at the RPBE level. Each panel displays 126 points.

https://dx.doi.org/10.1021/acs.jpca.0c06372
J. Phys. Chem. A 2020, 124, 10312−10323

hybrid PBE0 functionals result in $\Delta_{RMS}(^{15}N)$ = 6.6 and 6.9 ppm, respectively.

The results of calculations of nitrogen magnetic shielding tensors reproduce the trends observed for ^{14}N, ^{17}O, and ^{35}Cl EFG tensors. DFT calculations on the RPBE-D2* and RPBE-TS* energy-minimized structures result in the best agreement between experimental and calculated magnetic shielding and EFG tensors (*N.B.*: for calculations of ^{14}N EFG tensors, several of the energy-minimized structures perform equally well). This observation supports the conclusion that the force fields parameterized using input from quadrupolar SSNMR data result in structures that are better representations of the molecular-level structures of these solids. This conclusion is further supported by the fact that the magnetic shielding and quadrupolar interactions are independent of one another and unique in origin.

3.6. Unit Cell Volumes. Calculations of unit cell volumes are important metrics for evaluating the performance of force field correction models because these quantities are sensitive to the treatment of intermolecular noncovalent interactions (See Tables S12 and S13 for the results of these calculations).[123−127] First, we calculate the unit cell volumes of the X23 test set of Reilly and Tkatchenko, which consists of 23 dispersion-bound and hydrogen-bonded systems (Figure 6, Table 3).[98,99] We limit our analysis to 20 materials from the X23 set for which room temperature crystal structures are known (i.e., we do not include calculations of the unit cell volumes of ammonia, carbon dioxide, and cyanamide). When no force field correction is included in the structural refinement, the resulting unit cell volumes are always far larger than the experimental values (average error of ca. 49%). Each of the four force field correction models overestimates the unit cell volumes on average, although the calculated volumes are closer to the experimental values than when no dispersion correction is included. The best agreement with experiment is obtained from structural refinements at the RPBE-D2 level, which results in an average error of 1.5%. Calculations at the RPBE-D2*, RPBE-TS*, and RPBE-TS levels result in average errors of 5.7, 12.9, and 14.9%, respectively.

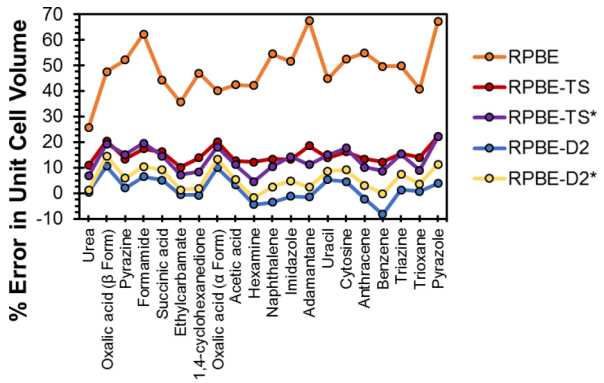

Figure 6. Percent errors in calculations of unit cell volumes for the X23 test set.

Table 3. Statistical Data for the Calculations of Unit Cell Volumes of the X23 and HCl15 Test Sets

	RPBE	RPBE-TS	RPBE-TS*	RPBE-D2	RPBE-D2*
X23 Test Set					
Avg[a]	48.5	14.9	12.9	1.5	5.7
Max(+)[b]	67.4	22.2	22.0	10.5	14.5
Max(−)[c]	25.5	10.1	4.6	−8.3	−1.8
Stdev[d]	10.1	3.3	4.9	4.7	4.6
HCl15 Test Set					
Avg[a]	20.0	11.4	6.6	3.9	3.1
Max(+)[b]	34.4	13.7	11.5	8.3	7.3
Max(−)[c]	−6.7	7.9	2.9	−0.2	−0.1
Stdev[d]	13.6	1.7	2.3	2.1	2.1

[a]Average percent error in unit cell volume. [b]Maximum positive percent error in unit cell volume. [c]Maximum negative percent error in unit cell volume. [d]Standard deviation for percent error in unit cell volume.

The unit cell volumes of 15 HCl salts (HCl15 test set) were also calculated (Figure 7, Table 3). In each case, comparison of calculated unit cell volumes was made with crystal structures that were determined at room temperature. When no force field correction is included in the geometry optimizations, the agreement with experiment is poor, with relative errors in volumes ranging between ca. −7 and 35%. The inclusion of any of the four force field corrections during the geometry optimizations brings the volumes into closer agreement with experiment, although each method overestimates the unit cell volumes. The best agreement with experiment is obtained from calculations performed at the RPBE-D2* and RPBE-D2 levels, with average errors of 3.1 and 3.9%, respectively. The RPBE-TS* and RPBE-TS methods lead to average errors of 6.6 and 11.4%, respectively, whereas calculations at the RPBE level (i.e., no force field correction) lead to an average error of 20.0%. The superior performance of the RPBE-TS* and RPBE-D2* methods for the prediction of unit cell volumes of HCl salts is consistent with our results for the predictions of ^{35}Cl EFG tensor parameters. In both cases, the successes of these methods are related to the ability to properly locate the positions of hydrogen atoms participating in hydrogen bonds with chloride ions: this is crucial for describing the energetics of the hydrogen bond and the ground-state electron density near the chlorine atom.

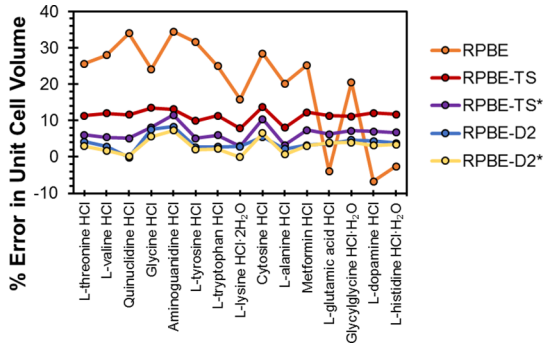

Figure 7. Percent errors in calculations of unit cell volumes for the HCl15 test set.

4. CONCLUSIONS

In this work, we have illustrated the optimization of the damping parameter within the Grimme and Tkatchenko−Scheffler two-body dispersion-corrected DFT schemes, to design force fields that are useful for refining the molecular-level structures of organic solids. The values of the damping parameters were optimized such that calculations on energy-

https://dx.doi.org/10.1021/acs.jpca.0c06372
J. Phys. Chem. A 2020, 124, 10312−10323

minimized structures result in agreement with experimentally derived EFG tensor parameters for ^{14}N, ^{17}O, and ^{35}Cl nuclear sites within the solids. The optimizations were accomplished through calculations of EFG tensor parameters on a training set of organic solids. Subsequently, the quality of the newly refined structures of a larger test set of organic solids was assessed for the calculations of EFG tensors, magnetic shielding tensors, and unit cell volumes.

Calculated EFG tensors are sensitive to very small variations and/or changes in molecular-level structures, making them invaluable for assessing the qualities of proposed crystal structures. Calculated values of EFG tensors associated with covalently bound atoms are impacted by the choice of energy-minimization method; however, ^{35}Cl EFG tensors of chloride ions are particularly sensitive to their local hydrogen bonding environments, making analyses of such sites powerful for NMR crystallography. Based on an analysis of 177 EFG tensors of ^{14}N, ^{17}O, and ^{35}Cl sites in a variety of molecular solids, we determine that structural refinements using the RPBE-TS* and RPBE-D2* methods result in better agreement with experimental EFG tensors than any other method explored herein, meaning that these calculations result in superior models of the actual molecular-level structures of the solids.

Calculated magnetic shielding tensors can also be used to assess the quality of a proposed crystal structure. We have calculated the magnetic shielding tensors of 42 nitrogen sites using both the GGA functional RPBE and the hybrid functional PBE0. In agreement with the results for the EFG tensors, the best agreement with experimental ^{15}N chemical shift tensors is obtained for RPBE-TS* and RPBE-D2* structures. Because the magnetic shielding and quadrupolar coupling interactions have independent physical origins, the combination of these two types of data gives further confidence to the validity of structures.

Finally, the energy-minimization methods were assessed for the prediction of unit cell volumes, as these quantities are useful metrics for assessing the accuracies of intermolecular noncovalent interactions in the calculations. This assessment is based on calculations on the X23 set of 23 molecular crystals, as well as a new database consisting of 15 hydrochloride organic salts (HCl15). For the X23 set, we find that the best agreement with experiment is found at the RPBE-D2 level; however, calculations at the RPBE-D2* and RPBE-TS* levels result in volumes that are intermediate to those obtained at the RPBE-D2 and RPBE-TS levels. For the HCl15 set, we find that both optimized force field corrections result in better predictions of unit cell volumes than the standard versions, and the best agreement with experiment is obtained at the RPBE-D2* level.

The results discussed in this study could have ramifications for the design of new or corrected force fields for the prediction, refinement, and/or validation of crystal structures. We have demonstrated that force fields developed using thermodynamic criteria (i.e., D2 and TS) can be improved upon by reoptimizing empirical parameters using calculations of anisotropic NMR interactions. In general, calculations on these new energy-minimized structures result in superior predictions of EFG and magnetic shielding tensor parameters while also resulting in unit cell volumes that are within the range established by the D2 and TS force fields. It is therefore possible that dispersion force fields could be designed through multiobjective optimizations to match both experimentally derived thermodynamic and NMR spectroscopic quantities.

■ ASSOCIATED CONTENT

Supporting Information

The Supporting Information is available free of charge at https://pubs.acs.org/doi/10.1021/acs.jpca.0c06372.

CIF files for all refined crystal structures (ZIP)

Atomic coordinates used in ADF calculations (ZIP)

Summary of all experimental and calculated NMR interaction parameters (PDF)

■ AUTHOR INFORMATION

Corresponding Author

Robert W. Schurko − *Department of Chemistry & Biochemistry, Florida State University, Tallahassee, Florida 32306, United States; National High Magnetic Field Laboratory, Tallahassee, Florida 32310, United States;* orcid.org/0000-0002-5093-400X; Phone: (850) 645-8614; Email: rschurko@fsu.edu

Authors

Sean T. Holmes − *Department of Chemistry & Biochemistry, Florida State University, Tallahassee, Florida 32306, United States; National High Magnetic Field Laboratory, Tallahassee, Florida 32310, United States*

Cameron S. Vojvodin − *Department of Chemistry & Biochemistry, Florida State University, Tallahassee, Florida 32306, United States; National High Magnetic Field Laboratory, Tallahassee, Florida 32310, United States*

Complete contact information is available at: https://pubs.acs.org/10.1021/acs.jpca.0c06372

Notes

The authors declare no competing financial interest.

■ ACKNOWLEDGMENTS

We thank Genentech, The Florida State University, the National High Magnetic Field Laboratory, and the Natural Sciences and Engineering Research Council of Canada (NSERC, RGPIN-2016_06642 Discovery Grant) for funding this research. The National High Magnetic Field Laboratory is supported by the National Science Foundation through NSF/DMR-1644779 and the State of Florida. This work was made possible, in part, by the facilities of the Shared Hierarchical Academic Research Computing Network (SHARCNET: www.sharcnet.ca).

■ REFERENCES

(1) Maddox, J. Crystals from first principles. *Nature* **1988**, *335*, 201−201.

(2) Beran, G. J. O.; Hartman, J. D.; Heit, Y. N. Predicting molecular crystal properties from first principles: finite-temperature thermochemistry to NMR crystallography. *Acc. Chem. Res.* **2016**, *49*, 2501−2508.

(3) van de Streek, J.; Neumann, M. A. Validation of experimental molecular crystal structures with dispersion-corrected density functional theory calculations. *Acta Crystallogr., Sect. B* **2010**, *66*, 544−558.

(4) Desiraju, G. R.; Steiner, T., *The Weak Hydrogen Bond in Structural Chemistry and Biology*. Oxford University Press, Inc.: New York, 1999.

(5) Desiraju, G. R. Cryptic crystallography. *Nat. Mater.* **2002**, *1*, 77−79.

(6) Grimme, S. Density functional theory with London dispersion corrections. *WIREs Comput. Mol. Sci.* **2011**, *1*, 211−228.

(7) Deringer, V. L.; George, J.; Dronskowski, R.; Englert, U. Plane-wave density functional theory meets molecular crystals: thermal ellipsoids and intermolecular interactions. *Acc. Chem. Res.* **2017**, *50*, 1231−1239.
(8) Hoja, J.; Reilly, A. M.; Tkatchenko, A. First-principles modeling of molecular crystals: structures and stabilities, temperature and pressure. *WIREs Comput. Mol. Sci.* **2017**, *7*, e1294.
(9) Kristyán, S.; Pulay, P. Can (semi)local density functional theory account for the London dispersion forces? *Chem. Phys. Lett.* **1994**, *229*, 175−180.
(10) Pérez-Jordá, J.; Becke, A. D. A density-functional study of van der Waals forces: rare gas diatomics. *Chem. Phys. Lett.* **1995**, *233*, 134−137.
(11) Oganov, A. R.; Pickard, C. J.; Zhu, Q.; Needs, R. J. Structure prediction drives materials discovery. *Nat. Rev. Mater.* **2019**, *4*, 331−348.
(12) Desiraju, G. R.; Vittal, J. J.; Ramanan, A., *Crystal Engineering: A Textbook*. World Scientific Publishing Co. Pte. Ltd.: Singapore, 2011.
(13) Nyman, J.; Day, G. M. Static and lattice vibrational energy differences between polymorphs. *CrystEngComm* **2015**, *17*, 5154−5165.
(14) Taylor, C. R.; Day, G. M. Evaluating the energetic driving force for cocrystal formation. *Cryst. Growth Des.* **2018**, *18*, 892−904.
(15) Harris, R. K.; Wasylishen, R. E.; Duer, M. J., *NMR Crystallography*. John Wiley & Sons Ltd: Singapore, 2009.
(16) Harper, J. K.; Grant, D. M. Enhancing crystal-structure prediction with NMR tensor data. *Cryst. Growth Des.* **2006**, *6*, 2315−2321.
(17) Kalakewich, K.; Iuliucci, R.; Harper, J. K. Establishing accurate high-resolution crystal structures in the absence of diffraction data and single crystals—an NMR approach. *Cryst. Growth Des.* **2013**, *13*, 5391−5396.
(18) Elena, B.; Emsley, L. Powder crystallography by proton solid-state NMR spectroscopy. *J. Am. Chem. Soc.* **2005**, *127*, 9140−9146.
(19) Elena, B.; Pintacuda, G.; Mifsud, N.; Emsley, L. Molecular structure determination in powders by NMR crystallography from proton spin diffusion. *J. Am. Chem. Soc.* **2006**, *128*, 9555−9560.
(20) Middleton, D. A.; Peng, X.; Saunders, D.; Shankland, K.; David, W. I. F.; Markvardsen, A. J. Conformational analysis by solid-state NMR and its application to restrained structure determination from powder diffraction data. *Chem. Commun.* **2002**, *17*, 1976−1977.
(21) Brouwer, D. H.; Cadars, S.; Eckert, J.; Liu, Z.; Terasaki, O.; Chmelka, B. F. A general protocol for determining the structures of molecularly ordered but noncrystalline silicate frameworks. *J. Am. Chem. Soc.* **2013**, *135*, 5641−5655.
(22) Brouwer, D. H. Structure solution of network materials by solid-state NMR without knowledge of the crystallographic space group. *Solid State Nucl. Magn. Reson.* **2013**, *51-52*, 37−45.
(23) Brouwer, D. H.; Horvath, M. A simulated annealing approach for solving zeolite crystal structures from two-dimensional NMR correlation spectra. *Solid State Nucl. Magn. Reson.* **2015**, *65*, 89−98.
(24) Salager, E.; Day, G. M.; Stein, R. S.; Pickard, C. J.; Elena, B.; Emsley, L. Powder crystallography by combined crystal structure prediction and high-resolution ^{1}H solid-state NMR spectroscopy. *J. Am. Chem. Soc.* **2010**, *132*, 2564−2566.
(25) Harper, J. K.; Barich, D. H.; Hu, J. Z.; Strobel, G. A.; Grant, D. M. Stereochemical analysis by solid-state NMR: structural predictions in ambuic acid. *J. Org. Chem.* **2003**, *68*, 4609−4614.
(26) Harper, J. K.; Tishler, D.; Richardson, D.; Lokvam, J.; Pendrill, R.; Widmalm, G. Solid-state NMR characterization of the molecular conformation in disordered ethyl α-l-rhamnofuranoside. *J. Phys. Chem. A* **2013**, *117*, 5534−5541.
(27) Baias, M.; Dumez, J. N.; Svensson, P. H.; Schantz, S.; Day, G. M.; Emsley, L. De novo determination of the crystal structure of a large drug molecule by crystal structure prediction-based powder NMR crystallography. *J. Am. Chem. Soc.* **2013**, *135*, 17501−17507.
(28) Baias, M.; Widdifield, C. M.; Dumez, J.-N.; Thompson, H. P. G.; Cooper, T. G.; Salager, E.; Bassil, S.; Stein, R. S.; Lesage, A.; Day, G. M.; Emsley, L. Powder crystallography of pharmaceutical materials by combined crystal structure prediction and solid-state ^{1}H NMR spectroscopy. *Phys. Chem. Chem. Phys.* **2013**, *15*, 8069−8080.
(29) Wang, L.; Uribe-Romo, F. J.; Mueller, L. J.; Harper, J. K. Predicting anisotropic thermal displacements for hydrogens from solid-state NMR: a study on hydrogen bonding in polymorphs of palmitic acid. *Phys. Chem. Chem. Phys.* **2018**, *20*, 8475−8487.
(30) Wang, W. D.; Gao, X. D.; Strohmeier, M.; Wang, W.; Bai, S.; Dybowski, C. Solid-state NMR studies of form I of atorvastatin calcium. *J. Phys. Chem. B.* **2012**, *116*, 3641−3649.
(31) Salager, E.; Stein, R. S.; Pickard, C. J.; Elena, B.; Emsley, L. Powder NMR crystallography of thymol. *Phys. Chem. Chem. Phys.* **2009**, *11*, 2610−2621.
(32) Holmes, S. T.; Iuliucci, R. J.; Mueller, K. T.; Dybowski, C. Density functional investigation of intermolecular effects on ^{13}C NMR chemical-shielding tensors modeled with molecular clusters. *J. Chem. Phys.* **2014**, *141*, 164121.
(33) Holmes, S. T.; Iuliucci, R. J.; Mueller, K. T.; Dybowski, C. Critical analysis of cluster models and exchange-correlation functionals for calculating magnetic shielding in molecular solids. *J. Chem. Theory Comput.* **2015**, *11*, 5229−5241.
(34) Alkan, F.; Holmes, S. T.; Dybowski, C. Role of exact exchange and relativistic approximations in calculating ^{19}F magnetic shielding in solids using a cluster ansatz. *J. Chem. Theory Comput.* **2017**, *13*, 4741−4752.
(35) Hartman, J. D.; Monaco, S.; Schatschneider, B.; Beran, G. J. O. Fragment-based ^{13}C nuclear magnetic resonance chemical shift predictions in molecular crystals: an alternative to planewave methods. *J. Chem. Phys.* **2015**, *143*, 102809.
(36) Hartman, J. D.; Kudla, R. A.; Day, G. M.; Mueller, L. J.; Beran, G. J. O. Benchmark fragment-based ^{1}H, ^{13}C, ^{15}N and ^{17}O chemical shift predictions in molecular crystals. *Phys. Chem. Chem. Phys.* **2016**, *18*, 21686−21709.
(37) Hartman, J. D.; Balaji, A.; Beran, G. J. O. Improved electrostatic embedding for fragment-based chemical shift calculations in molecular crystals. *J. Chem. Theory Comput.* **2017**, *13*, 6043−6051.
(38) Hartman, J. D.; Beran, G. J. O. Accurate ^{13}C and ^{15}N molecular crystal chemical shielding tensors from fragment-based electronic structure theory. *Solid State Nucl. Magn. Reson.* **2018**, *96*, 10−18.
(39) Holmes, S. T.; Engl, O. G.; Srnec, M. N.; Madura, J. D.; Quiñones, R.; Harper, J. K.; Schurko, R. W.; Iuliucci, R. J. Chemical shift tensors of cimetidine form A modeled with density functional theory calculations: implications for NMR crystallography. *J. Phys. Chem. A* **2020**, *124*, 3109−3119.
(40) Hartman, J. D.; Day, G. M.; Beran, G. J. O. Enhanced NMR discrimination of pharmaceutically relevant molecular crystal forms through fragment-based ab initio chemical shift predictions. *Cryst. Growth Des.* **2016**, *16*, 6479−6493.
(41) Widdifield, C. M.; Farrell, J. D.; Cole, J. C.; Howard, J. A. K.; Hodgkinson, P. Resolving alternative organic crystal structures using density functional theory and NMR chemical shifts. *Chem. Sci.* **2020**, *11*, 2987.
(42) Harper, J. K.; Iuliucci, R.; Gruber, M.; Kalakewich, K. Refining crystal structures with experimental ^{13}C NMR shift tensors and lattice-including electronic structure methods. *CrystEngComm* **2013**, *15*, 8693−8704.
(43) Harris, R. K.; Hodgkinson, P.; Pickard, C. J.; Yates, J. R.; Zorin, V. Chemical shift computations on a crystallographic basis: some reflections and comments. *Magn. Reson. Chem.* **2007**, *45*, S174−S186.
(44) Hodgkinson, P. NMR crystallography of molecular organics. *Prog. Nucl. Magn. Reson. Spectrosc.* **2020**, *118-119*, 10−53.
(45) Ashbrook, S. E.; McKay, D. Combining solid-state NMR spectroscopy with first-principles calculations - a guide to NMR crystallography. *Chem. Commun.* **2016**, *52*, 7186−7204.
(46) Perras, F. A.; Bryce, D. L. Multinuclear magnetic resonance crystallographic structure refinement and cross-validation using experimental and computed electric field gradients: application to $Na_2Al_2B_2O_7$. *J. Phys. Chem. C* **2012**, *116*, 19472−19482.
(47) O'Dell, L. A.; Schurko, R. W.; Harris, K. J.; Autschbach, J.; Ratcliffe, C. I. Interaction tensors and local dynamics in common

structural motifs of nitrogen: a solid-state ^{14}N NMR and DFT study. *J. Am. Chem. Soc.* **2011**, *133*, 527−546.
(48) O'Dell, L. A.; Ratcliffe, C. I.; Kong, X.; Wu, G. Multinuclear solid-state nuclear magnetic resonance and density functional theory characterization of interaction tensors in taurine. *J. Phys. Chem. A* **2012**, *116*, 1008−1014.
(49) Veinberg, S. L.; Friedl, Z. W.; Harris, K. J.; O'Dell, L. A.; Schurko, R. W. Ultra-wideline ^{14}N solid-state NMR as a method for differentiating polymorphs: glycine as a case study. *CrystEngComm* **2015**, *17*, 5225−5236.
(50) Veinberg, S. L.; Friedl, Z. W.; Lindquist, A. W.; Kispal, B.; Harris, K. J.; O'Dell, L. A.; Schurko, R. W. ^{14}N solid-state NMR spectroscopy of amino acids. *ChemPhysChem* **2016**, *17*, 4011−4027.
(51) Veinberg, S. L.; Johnston, K. E.; Jaroszewicz, M. J.; Kispal, B. M.; Mireault, C. R.; Kobayashi, T.; Pruski, M.; Schurko, R. W. Natural abundance ^{14}N and ^{15}N solid-state NMR of pharmaceuticals and their polymorphs. *Phys. Chem. Chem. Phys.* **2016**, *18*, 17713−17730.
(52) Harbison, G. S.; Kye, Y.-S.; Penner, G. H.; Grandin, M.; Monette, M. ^{14}N quadrupolar, ^{14}N and ^{15}N chemical shift, and ^{14}N−^{1}H dipolar tensors of sulfamic acid. *J. Phys. Chem. B* **2002**, *106*, 10285−10291.
(53) Naito, A.; Ganapathy, S.; Raghunathan, P.; McDowell, C. A. Determination of the nitrogen-14 quadrupole coupling tensor and the carbon-13 chemical shielding tensors in a single crystal of L-serine monohydrate. *J. Chem. Phys.* **1983**, *79*, 4173−4182.
(54) Naito, A.; McDowell, C. A. Determination of the nitrogen-14 quadrupole coupling tensors and the carbon-13 chemical shielding tensors in a single crystal of L-asparagine monohydrate. *J. Chem. Phys.* **1984**, *81*, 4795−4803.
(55) McDowell, C. A.; Naito, A.; Sastry, D. L.; Takegoshi, K. Determination of the ^{14}N quadrupole coupling tensors in a single crystal of L-histidine hydrochloride monohydrate by NMR spectroscopy. *J. Magn. Reson.* **1986**, *69*, 283−292.
(56) Garcia, M. L. S.; Smith, J. A. S. ^{14}N and ^{2}H quadrupole double resonance in salts of cytosine and adenine. *J. Chem. Soc., Perkin Trans.* **1983**, *2*, 1401−1408.
(57) Garcia, M. L. S.; Smith, J. A. S.; Bavin, P. M. G.; Ganellin, C. R. ^{14}N and ^{2}H quadrupole double resonance in substituted imidazoles. *J. Chem. Soc., Perkin Trans.* **1983**, *2*, 1391−1399.
(58) Yesinowski, J. P.; Buess, M. L.; Garroway, A. N.; Ziegeweid, M.; Pines, A. Detection of ^{14}N and ^{35}Cl in cocaine base and hydrochloride using NQR, NMR, and SQUID techniques. *Anal. Chem.* **1995**, *67*, 2256−2263.
(59) Harris, K. J.; Veinberg, S. L.; Mireault, C. R.; Lupulescu, A.; Frydman, L.; Schurko, R. W. Rapid acquisition of ^{14}N solid-state NMR spectra with broadband cross polarization. *Chem. − Eur. J.* **2013**, *19*, 16469−16475.
(60) Wu, G. Solid-State ^{17}O NMR studies of organic and biological molecules: recent advances and future directions. *Solid State Nucl. Magn. Reson.* **2016**, *73*, 1−14.
(61) Dong, S.; Ida, R.; Wu, G. A combined experimental and theoretical ^{17}O NMR study of crystalline urea: an example of large hydrogen-bonding effects. *J. Phys. Chem. A* **2000**, *104*, 11194−11202.
(62) Dong, S.; Yamada, K.; Wu, G. Oxygen-17 nuclear magnetic resonance of organic solids. *Z. Naturforsch.* **2000**, *55*, 21−28.
(63) Kong, X.; O'Dell, L. A.; Terskikh, V.; Ye, E.; Wang, R.; Wu, G. Variable-temperature ^{17}O NMR studies allow quantitative evaluation of molecular dynamics in organic solids. *J. Am. Chem. Soc.* **2012**, *134*, 14609−14617.
(64) Kong, X.; Shan, M.; Terskikh, V.; Hung, I.; Gan, Z.; Wu, G. Solid-State ^{17}O NMR of pharmaceutical compounds: salicylic acid and aspirin. *J. Phys. Chem. B* **2013**, *117*, 9643−9654.
(65) Kong, X.; Terskikh, V.; Toubaei, A.; Wu, G. A solid-state ^{17}O NMR study of platinum-carboxylate complexes: carboplatin and oxaliplatin. *Can. J. Chem.* **2015**, *93*, 945−953.
(66) Wu, G.; Dong, S.; Ida, R.; Reen, N. A solid-state ^{17}O nuclear magnetic resonance study of nucleic acid bases. *J. Am. Chem. Soc.* **2002**, *124*, 1768−1777.
(67) Wu, G.; Mason, P.; Mo, X.; Terskikh, V. Experimental and computational characterization of the ^{17}O quadrupole coupling and magnetic shielding tensors for p-nitrobenzaldehyde and formaldehyde. *J. Phys. Chem. A* **2008**, *112*, 1024−1032.
(68) Nozik, Y. Z.; Fykin, L. E.; Muradyan, L. A. Refinement of Crystal-Structure of Cotunnite, Pbcl-2, by Neutron-Diffraction Method. *Kristallografiya* **1976**, *21*, 76−79.
(69) Pike, K. J.; Lemaitre, V.; Kukol, A.; Anupõld, T.; Samoson, A.; Howes, A. P.; Watts, A.; Smith, M. E.; Dupree, R. Solid-state ^{17}O NMR of amino acids. *J. Phys. Chem. B* **2004**, *108*, 9256−9263.
(70) Scheubel, W.; Zimmermann, H.; Haeberlen, U. ^{17}O quadrupole coupling and nuclear magnetic shielding tensors in benzophenone. *J. Magn. Reson.* **1985**, *63*, 544−555.
(71) Lemaitre, V.; Pike, K. J.; Watts, A.; Anupold, T.; Samoson, A.; Smith, M. E.; Dupree, R. New insights into the bonding arrangements of L- and D-glutamates from solid state ^{17}O NMR. *Chem. Phys. Lett.* **2003**, *371*, 91−97.
(72) Brosnan, S. G. P.; Edmonds, D. T.; Poplett, I. J. F. An ^{17}O nuclear quadrupole resonance study of some carboxylic acids. *J. Magn. Reson.* **1981**, *45*, 451−460.
(73) Kuroki, S.; Takahashi, A.; Ando, I.; Shoji, A.; Ozaki, T. Hydrogen-bonding structural study of solid peptides and polypeptides containing a glycine residue by ^{17}O NMR spectroscopy. *J. Mol. Struct.* **1994**, *323*, 197−208.
(74) Poplett, I. J. F.; Smith, J. A. S. ^{17}O and ^{2}H quadrupole double resonance in some carboxylic acid dimers. *J. Chem. Soc., Faraday Trans.* **1981**, *77*, 1473−1485.
(75) Gann, S. L.; Baltisberger, J. H.; Wooten, E. W.; Zimmermann, H.; Pines, A. Cross polarization and dynamic-angle spinning of ^{17}O in L-alanine. *Bull. Magn. Reson.* **1994**, *16*, 68−72.
(76) Zhang, Q.; Chekmenev, E. Y.; Wittebort, R. J. ^{17}O quadrupole coupling and chemical shielding tensors in an H-bonded carboxyl group: α-oxalic acid. *J. Am. Chem. Soc.* **2003**, *125*, 9140−9146.
(77) Zhang, Q. W.; Zhang, H. M.; Usha, M. G.; Wittebort, R. J. ^{17}O NMR and crystalline hydrates. *Solid State Nucl. Magn. Reson.* **1996**, *7*, 147−154.
(78) Bryce, D. L.; Gee, M.; Wasylishen, R. E. High-field chlorine NMR spectroscopy of solid organic hydrochloride salts: a sensitive probe of hydrogen bonding environments. *J. Phys. Chem. A* **2001**, *105*, 10413−10421.
(79) Hamaed, H.; Pawlowski, J. M.; Cooper, B. F. T.; Fu, R.; Eichhorn, S. H.; Schurko, R. W. Application of solid-state ^{35}Cl NMR to the structural characterization of hydrochloride pharmaceuticals and their polymorphs. *J. Am. Chem. Soc.* **2008**, *130*, 11056−11065.
(80) Hirsh, D. A.; Holmes, S. T.; Chakravarty, P.; Peach, A. A.; DiPasquale, A. G.; Nagapudi, K.; Schurko, R. W. *In situ* characterization of waters of hydration in a variable-hydrate active pharmaceutical ingredient using ^{35}Cl solid-state NMR and X-ray diffraction. *Cryst. Growth Des.* **2019**, *19*, 7349−7362.
(81) Peach, A. A.; Hirsh, D. A.; Holmes, S. T.; Schurko, R. W. Mechanochemical syntheses and ^{35}Cl solid-state NMR characterization of fluoxetine HCl cocrystals. *CrystEngComm* **2018**, *20*, 2780−2792.
(82) Bryce, D. L.; Sward, G. D.; Adiga, S. Solid-state $^{35/37}$Cl NMR spectroscopy of hydrochloride salts of amino acids implicated in chloride ion transport channel selectivity: opportunities at 900 MHz. *J. Am. Chem. Soc.* **2006**, *128*, 2121−2134.
(83) Chapman, R. P.; Bryce, D. L. A high-field solid-state $^{35/37}$Cl NMR and quantum chemical investigation of the chlorine quadrupolar and chemical shift tensors in amino acid hydrochlorides. *Phys. Chem. Chem. Phys.* **2007**, *9*, 6219−6230.
(84) Hildebrand, M.; Hamaed, H.; Namespetra, A. M.; Donohue, J. M.; Fu, R.; Hung, I.; Gan, Z.; Schurko, R. W. ^{35}Cl solid-state NMR of HCl salts of active pharmaceutical ingredients: structural prediction, spectral fingerprinting and polymorph recognition. *CrystEngComm* **2014**, *16*, 7334−7356.
(85) Namespetra, A. M.; Hirsh, D. A.; Hildebrand, M. P.; Sandre, A. R.; Hamaed, H.; Rawson, J. M.; Schurko, R. W. ^{35}Cl solid-state NMR

spectroscopy of HCl pharmaceuticals and their polymorphs in bulk and dosage forms. *CrystEngComm* **2016**, *18*, 6213−6232.
(86) Attrell, R. J.; Widdifield, C. M.; Korobkov, I.; Bryce, D. L. Weak halogen bonding in solid haloanilinium halides probed directly via chlorine-35, bromine-81, and iodine-127 NMR spectroscopy. *Cryst. Growth Des.* **2012**, *12*, 1641−1653.
(87) Hirsh, D. A.; Rossini, A. J.; Emsley, L.; Schurko, R. W. ^{35}Cl dynamic nuclear polarization solid-state NMR of active pharmaceutical ingredients. *Phys. Chem. Chem. Phys.* **2016**, *18*, 25893−25904.
(88) Vogt, F. G.; Williams, G. R.; Copley, R. C. B. Solid-state NMR analysis of a boron-containing pharmaceutical hydrochloride salt. *J. Pharm. Sci.* **2013**, *102*, 3705−3716.
(89) Paulekuhn, G. S.; Dressman, J. B.; Saal, C. Trends in active pharmaceutical ingredient salt selection based on analysis of the orange book database. *J. Med. Chem.* **2007**, *50*, 6665−6672.
(90) Dolgonos, G. A.; Boese, A. D. Adjusting dispersion parameters for the density-functional tight-binding description of molecular crystals. *Chem. Phys. Lett.* **2019**, *718*, 7−11.
(91) Strutyński, K.; Melle-Franco, M.; Gomes, J. A. N. F. New parameterization scheme of DFT-D for graphitic materials. *J. Phys. Chem. A* **2013**, *117*, 2844−2853.
(92) Civalleri, B.; Zicovich-Wilson, C. M.; Valenzano, L.; Ugliengo, P. B3LYP augmented with an empirical dispersion term (B3LYP-D*) as applied to molecular crystals. *CrystEngComm* **2008**, *10*, 405−410.
(93) Jurečka, P.; Černý, J.; Hobza, P.; Salahub, D. R. Density functional theory augmented with an empirical dispersion term. interaction energies and geometries of 80 noncovalent complexes compared with ab initio quantum mechanics calculations. *J. Comput. Chem.* **2007**, *28*, 555−569.
(94) Holmes, S. T.; Iuliucci, R. J.; Mueller, K. T.; Dybowski, C. Semi-empirical refinements of crystal structures using ^{17}O quadrupolar-coupling tensors. *J. Chem. Phys.* **2017**, *146*, No. 064201.
(95) Holmes, S. T.; Schurko, R. W. Refining crystal structures with quadrupolar NMR and dispersion-corrected density functional theory. *J. Phys. Chem. C* **2018**, *122*, 1809−1820.
(96) Grimme, S. Semiempirical GGA-type density functional constructed with a long-range dispersion correction. *J. Comput. Chem.* **2006**, *27*, 1787−1799.
(97) Tkatchenko, A.; Scheffler, M. Accurate molecular van der Waals interactions from ground-state electron density and free-atom reference data. *Phys. Rev. Lett.* **2009**, *102*, No. 073005.
(98) Reilly, A. M.; Tkatchenko, A. Understanding the role of vibrations, exact exchange, and many-body van der Waals interactions in the cohesive properties of molecular crystals. *J. Chem. Phys.* **2013**, *139*, No. 024705.
(99) Reilly, A. M.; Tkatchenko, A. Seamless and accurate modeling of organic molecular materials. *J. Phys. Chem. Lett.* **2013**, *4*, 1028−1033.
(100) Clark, S. J.; Segall, M. D.; Pickard, C. J.; Hasnip, P. J.; Probert, M. J.; Refson, K.; Payne, M. C. First principles methods using CASTEP. *Z. Kristallogr.* **2005**, *220*, 567−570.
(101) Bonhomme, C.; Gervais, C.; Babonneau, F.; Coelho, C.; Pourpoint, F.; Azais, T.; Ashbrook, S. E.; Griffin, J. M.; Yates, J. R.; Mauri, F.; Pickard, C. J. First-principles calculation of NMR parameters using the gauge including projector augmented wave method: a chemist's point of view. *Chem. Rev.* **2012**, *112*, 5733−5779.
(102) Pfrommer, B. G.; Côté, M.; Louie, S. G.; Cohen, M. L. Relaxation of crystals with the quasi-Newton method. *J. Comput. Phys.* **1997**, *131*, 233−240.
(103) Hammer, B.; Hansen, L. B.; Nørskov, J. K. Improved adsorption energetics within density-functional theory using revised Perdew-Burke-Ernzerhof functionals. *Phys. Rev. B* **1999**, *59*, 7413−7421.
(104) Holmes, S. T.; Alkan, F.; Iuliucci, R. J.; Mueller, K. T.; Dybowski, C. Analysis of the bond-valence method for calculating ^{29}Si and ^{31}P magnetic shielding in covalent network solids. *J. Comput. Chem.* **2016**, *37*, 1704−1710.
(105) Holmes, S. T.; Bai, S.; Iuliucci, R. J.; Mueller, K. T.; Dybowski, C. Calculations of solid-state ^{43}Ca NMR parameters: a comparison of periodic and cluster approaches and an evaluation of DFT functionals. *J. Comput. Chem.* **2017**, *38*, 949−956.
(106) Yates, J. R.; Pickard, C. J.; Mauri, F. Calculation of NMR chemical shifts for extended systems using ultrasoft pseudopotentials. *Phys. Rev. B* **2007**, *76*, No. 024401.
(107) McNellis, E. R.; Meyer, J.; Reuter, K. Azobenzene at coinage metal surfaces: role of dispersive van der Waals interactions. *Phys. Rev. B* **2009**, *80*, 205414.
(108) Profeta, M.; Mauri, F.; Pickard, C. J. Accurate first principles prediction of ^{17}O NMR parameters in SiO_2: assignment of the zeolite ferrierite spectrum. *J. Am. Chem. Soc.* **2003**, *125*, 541−548.
(109) Pickard, C. J.; Mauri, F. All-electron magnetic response with pseudopotentials: NMR chemical shifts. *Phys. Rev. B* **2001**, *63*, 245101.
(110) Schreckenbach, G.; Ziegler, T. Calculation of NMR shielding tensors using gauge-including atomic orbitals and modern density functional theory. *J. Phys. Chem.* **1995**, *99*, 606−611.
(111) Adamo, C.; Barone, V. Toward reliable density functional methods without adjustable parameters: the PBE0 model. *J. Chem. Phys.* **1999**, *110*, 6158−6170.
(112) Pyykkö, P. Spectroscopic nuclear quadrupole moments. *Mol. Phys.* **2001**, *99*, 1617−1629.
(113) Liu, F.; Phung, C. G.; Alderman, D. W.; Grant, D. M. Analyzing and assigning carbon-13 chemical-chift tensors in fructose, sorbose, and xylose single crystals. *J. Magn. Reson.* **1996**, *120*, 231.
(114) Price, D. L.; Skold, K., Introduction to Neutron Scattering. In *Methods in Experimental Physics*, Sköld, K.; Price, D. L., Eds. Academic Press: 1986; *23*, 1−97.
(115) Al-Karaghouli, A. R.; Cole, F. E.; Lehmann, M. S.; Miskell, C. F.; Verbist, J. J.; Koetzle, T. F. Precision neutron diffraction structure determination of protein and nucleic acid components. XVII. molecular and crystal structure of the amino acid glycine hydrochloride LORIDE. *J. Chem. Phys.* **1975**, *63*, 1360−1366.
(116) Al-Karaghouli, A. R.; Koetzle, T. F. Neutron diffraction study of L-phenylalanine hydrochloride. *Acta Crystallogr., Sect. B* **1975**, *31*, 2461−2465.
(117) Koetzle, T. F.; Golic, L.; Lehmann, M. S.; Verbist, J. J.; Hamilton, W. C. Precision neutron diffraction structure determination of protein and nucleic acid components.xv. Crystal and molecular structure of the amino acid L-valine hydrochloride. *J. Chem. Phys.* **1974**, *60*, 4690−4696.
(118) Koetzle, T. F.; Lehmann, M. S.; Verbist, J. J.; Hamilton, W. C. Precision neutron diffraction structure determination of protein and nucleic acid components. vii. the crystal and molecular structure of the amino acid L-lysine monohydrochloride dihydrate. *Acta Crystallogr., Sect. B* **1972**, *28*, 3207−3214.
(119) Sequeira, A.; Rajagopal, H.; Chidambaram, R. A neutron diffraction study of the structure of L-glutamic acid·HCl. *Acta Crystallogr., Sect. B* **1972**, *28*, 2514−2519.
(120) Fuess, H.; Hohlwein, D.; Mason, S. A. Neutron diffraction study of L-histidine hydrochloride monohydrate. *Acta Crystallogr., Sect. B* **1977**, *33*, 654−659.
(121) Bugayong, R. R.; Sequeira, A.; Chidambaram, R. A neutron diffraction study of the structure of L-lysine monohydrochloride dihydrate. *Acta Crystallogr., Sect. B* **1972**, *28*, 3214−3219.
(122) van de Streek, J.; Neumann, M. A. Validation of molecular crystal structures from powder diffraction data with dispersion-corrected density functional theory (DFT-D). *Acta Crystallogr., Sect. B* **2014**, *70*, 1020−1032.
(123) Dolgonos, G. A.; Hoja, J.; Boese, A. D. Revised values for the X23 benchmark set of molecular crystals. *Phys. Chem. Chem. Phys.* **2019**, *21*, 24333−24344.
(124) Moellmann, J.; Grimme, S. DFT-D3 study of some molecular crystals. *J. Phys. Chem. C* **2014**, *118*, 7615−7621.
(125) Thomas, S. P.; Spackman, P. R.; Jayatilaka, D.; Spackman, M. A. Accurate lattice energies for molecular crystals from experimental crystal structures. *J. Chem. Theory Comput.* **2018**, *14*, 1614−1623.
(126) Cutini, M.; Civalleri, B.; Corno, M.; Orlando, R.; Brandenburg, J. G.; Maschio, L.; Ugliengo, P. Assessment of different

quantum mechanical methods for the prediction of structure and cohesive energy of molecular crystals. *J. Chem. Theory Comput.* **2016**, *12*, 3340−3352.
(127) Loboda, O. A.; Dolgonos, G. A.; Boese, A. D. Towards hybrid density functional calculations of molecular crystals via fragment-based methods. *J. Chem. Phys.* **2018**, *149*, 124104.

https://dx.doi.org/10.1021/acs.jpca.0c06372
J. Phys. Chem. A 2020, 124, 10312−10323